Design of a Stable Heusler Alloy with Switchable Metal-to-Half-Metal Transition at Finite Temperature

Buchelnikov Vasiliy D., Sokolovskiy Vladimir V., Miroshkina Olga N., Baigutlin Danil R., Zagrebin Mikhail A., Barbiellini Bernardo, Singh Bahadur, Bansil Arun, Lähderanta Erkki

Design of a stable Heusler alloy with switchable metal-to-half-metal transition at finite temperature

Vasiliy D. Buchelnikov* Vladimir V. Sokolovskiy Olga N. Miroshkina Danil R. Baigutlin Mikhail A. Zagrebin Bernardo Barbiellini Bahadur Singh Arun Bansil Erkki Lähderanta

Vasiliy D. Buchelnikov, Vladimir V. Sokolovskiy, Olga N. Miroshkina, Danil R. Baigutlin, Mikhail A. Zagrebin
Faculty of Physics, Chelyabinsk State University, 454001 Chelyabinsk, Russia
Email Address: buche@csu.ru
Danil R. Baigutlin, Bernardo Barbiellini, Erkki Lähderanta
Physics Department, School of Engineering Science, LUT-University, FI-53851 Lappeenranta, Finland
Olga N. Miroshkina
Faculty of Physics and Center for Nanointegration Duisburg-Essen (CENIDE), University of Duisburg-Essen, 47057, Duisburg, Germany
Mikhail A. Zagrebin
National Research South Ural State University, 454080 Chelyabinsk, Russia
Bernardo Barbiellini, Arun Bansil
Physics Department, Northeastern University, Boston, Massachusetts 02115, USA
Bahadur Singh
Department of Condensed Matter Physics and Materials Science, Tata Institute of Fundamental Research, Colaba, Mumbai 400005, India

We discuss the electronic structure and metallicity of Si-doped Mn_2VGe Heusler alloys within the first-principles density-functional theory framework. Mn_2VGe is found to assume two stable structures at (cubic) lattice constants of 5.7 and 6.05 Å, which are well separated in energy and correspond to half-metallic (low-spin) and metallic (high-spin) phases, respectively. Substitution of Ge by Si reduces the energy difference between these two phases, which become nearly degenerate at a Si concentration of $\approx$ 3.125 at.% at zero temperature. Our analysis shows that the switching between the high- and low-spin phases for this composition could be triggered via a pressure of 2.8 GPa at 300 K. Si-doped Mn_2VGe could thus provide an ultrafast, low power, cost-effective materials platform for spintronics applications.

1 Introduction

Half-metallic (HM) materials are continuing to attract interest due to their potential spintronics applications involving novel thermoelectrics, spin filters, data storage and other spin-based devices [1, 2, 3, 4]. The HMs exhibit metallic behavior in one spin channel and semiconducting behavior in the other spin channel around the Fermi energy (E_F). Predictions of HM band structures have been made in many materials, including the magnetic oxides [5], diluted magnetic semiconductors [6] and the Heusler alloys [7, 8, 9]. The full Heusler compounds given by the chemical formula X_2YZ, where X and Y are transition metals and Z is a main group element, present an especially large materials family with tunable electronic structures, high spin polarizations and Curie temperatures, and good thermoelectric performance, among other interesting properties.

Mn_2-based Heusler alloys with half-metallic or spin-gapless semiconducting properties are particularly interesting as they host Mn^{3+} ions with d^4 electronic configuration and strong ferromagnetic (FM) as well as antiferromagnetic (AFM) correlations between the Mn atoms. As a result, these alloys have low magnetic moments and reduced stray fields, making them promising materials for spintronics applications. Mn_2VAl was the first to be proposed as a HM ferromagnet and it has been thoroughly investigated both experimentally [10] and theoretically [11, 12]. Other examples include Mn_2VAl, Mn_2VSi, Mn_2FeZ (Z = Al, Sb), Mn_2CoZ (Z = Al, Ga, Si, Sb), Mn_2CuSb, and Mn_2ZrSi [11, 13, 14, 15, 16, 17, 18, 19, 20, 21, 22, 23]. Notably, using x-ray diffraction and SQUID magnetometry, Jiang *et al.* [10] showed that in Mn_2VAl, the magnetic moment at 5 K is 1.94 μ_B/f.u., which is well-aligned with the Slater-Pauling (SP)

rule. Also, Kumar *et al.* [24] synthesized Mn$_2$VGa and reported half-metallicity using electrical resistivity measurements.

Theoretical studies have been performed with DFT (density-functional theory) within the local-spin-density approximation (LSDA) [25] and the generalized-gradient approximation (GGA) [26, 27, 28]. In contrast to the GGA, the LSDA does not predict the HM behavior in Mn$_2$-based Heusler alloys. However, Özdoğan *et al.* [13] report that a small expansion of the LSDA-obtained equilibrium volume induces half-metallicity in Mn$_2$VZ (Z = Al, Ge, Si, Ga, In, Sn) compounds with a high degree of spin polarization at the E_F. Moreover, these compounds exhibit ferrimagnetism with antiparallel alignment of Mn and V spins. Substitution of a small amount of V by Si in Mn$_2$VSi preserves the high degree of spin polarization although the total magnetic moment is reduced substantially. Galanakis *et al.* [29] studied the effect of partial Co and Fe substitution for Mn in the HM antiferromagnets Mn$_2$VAl and Mn$_2$VSi and found that Fe or Co doping does not destroy the HM character of the parent compounds. The inverse Heusler (Hg$_2$CuTi-type) structure and HM ferrimagnetic (FIM) nature of Mn$_2$CoZ (Z= Al, Si, Ge, Sn, and Sb) have been predicted theoretically and confirmed experimentally by Liu *et al.* [30]. Luo *et al.* [14] show that Mn$_2$FeAl and Mn$_2$FeSb are HM ferromagnets among the Mn$_2$FeZ family (Z = Al, Ga, Si, Ge, Sb). FIM HM character has been reported for Mn$_2$CuZ (Z = Al, Si, Ge) [31, 32, 33] within the inverse Heusler structure. FM HM character and the possibility of a tetragonal martensitic transformation in Mn$_2$Rh(Si, Ge) with the regular (Cu$_2$MnAl-type) Heusler structure have been predicted by Bensaid *et al.* [34]. Ram *et al.* [35] studied Mn$_2$ScZ(Z = Si, Ge, Sn) assuming on-site Coulomb interaction effects and concluded that the HM behavior with narrow band gap is found only when Z is Si or Ge. Recently, we reported that the implementation of electron correlation effects using the strongly-constrained-and-appropriately-normed (SCAN) meta-GGA functional [36, 37] yields nearly degenerate HM and metallic phases in Mn$_2$ScSi, in contrast to the results of Ram *et al.* [35]. It has been suggested that switching between these two phases could be achieved by applying volume change within the cubic phase or by the application of an external magnetic field [38]. However, our phase stability analysis shows that Mn$_2$ScSi is metastable against decomposition into stable components. Also, the high cost of Sc will limit the use of Mn$_2$ScSi in applications.

We note that the meta-GGA SCAN functional, which takes into account kinetic energy density, has proven its efficacy for a wide range diversely-bonded materials, including intermediate-range van-der-Waals interactions [37], ionic bonding [39], and covalent and metallic bonds [37]. SCAN has been shown to capture correctly the lattice constants of 2D [40] and highly correlated materials [41, 42, 43]. In a recent study we showed that in contrast to the PBE, SCAN predicts correctly the non-collinear magnetic structure and equilibrium volume of α-Mn [44]. In Ni$_2$MnGa, SCAN yields [45] a tetragonal ratio of $c/a = 1.20$, which is close to the experimental $c/a = 1.18 \pm 0.02$ compared to the PBE value $c/a = 1.25$. In half-metallic systems [46], SCAN yields the correct gap at the Fermi level and the integral value of the magnetic moment in keeping with the half-metallic character of Co$_2$FeSi, where the PBE fails.

Our study aims to provide a detailed theoretical description of a promising Mn-V-Ge full-Heusler alloy, which is shown to demonstrate a switchable low (LMS) to high magnetic state (HMS) behavior. We show that such a switching mechanism can be treated via the exchange-correlation effects described within the SCAN functional. Stoichiometric Mn$_2$VGe is found to display an energy difference between the LMS and HMS phases, which is too large to allow easy switching between these two phases. For this reason, we explore the effects of small Si doping, which drives the LMS and HMS phases into near degeneracy. In this way, Si doping significantly decreases the external pressure needed for switching. In contrast to Mn$_2$ScSi, the Si-doped Mn$_2$VGe alloys are more cost effective and found to be stable to segregation.

An outline of this paper is as follows. Sec. II gives details of the calculations. Sec. III is devoted to the discussion of the results of structural, magnetic, and electronic properties and phase stability of Mn$_2$VGe. Conclusion are presented in Sec. IV.
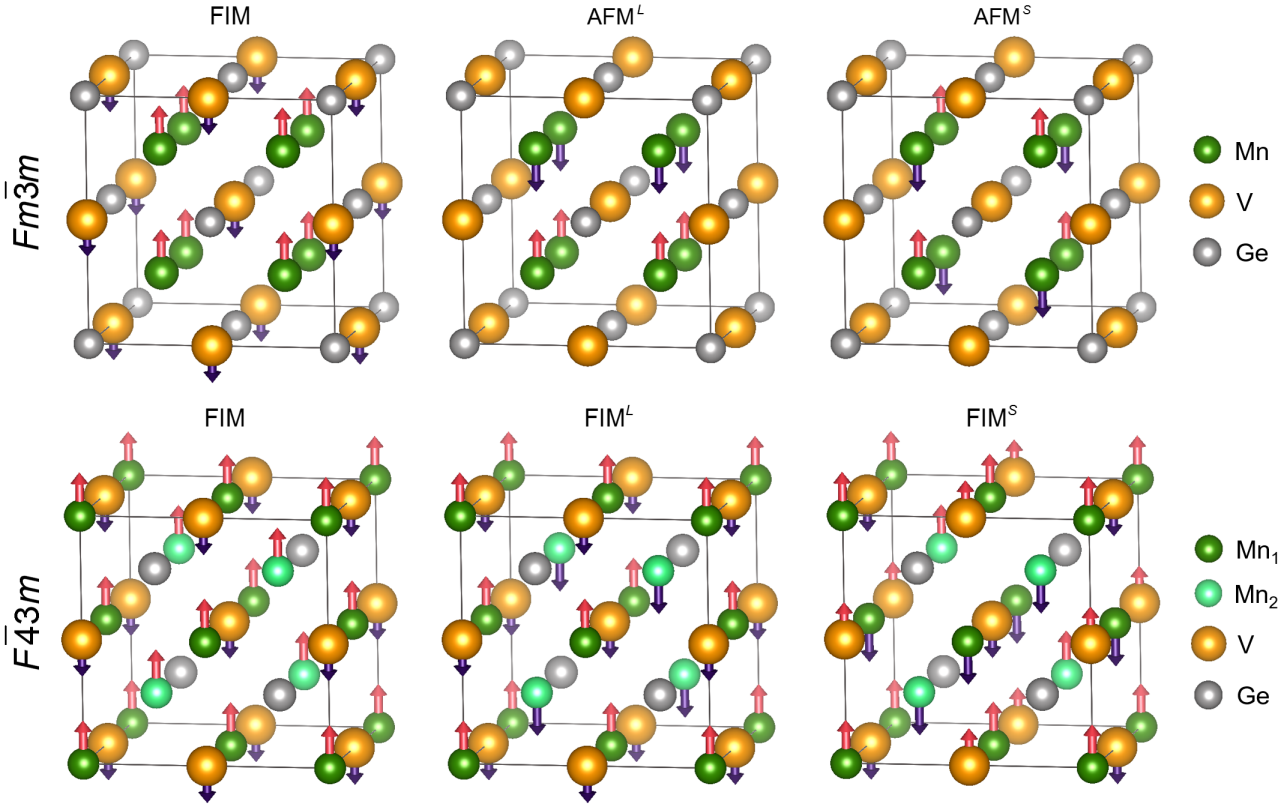
Figure 1: Regular $Fm\bar{3}m$ (top panel) and inverse $F\bar{4}3m$ (bottom panel) Heusler structures used in calculations. For the regular structure: FIM order denotes the spin configuration with reversed V magnetic moment (μ_V) with respect to that for Mn (μ_{Mn}); AFM order is the antiferromagnetic alignment of μ_{Mn}, while μ_V equals zero. For the inverse structure: FIM order refers to the configuration with reversed μ_V with respect to all Mn moments; FIM^{L,S} orders denote the ferrimagnetic configurations with antiparallel alignment of Mn atoms and non-zero μ_V. Here, the superscript L corresponds to the layer-by-layer ordering, and the superscript S corresponds to the staggered ordering of the Mn magnetic moments.

2 Computational Details

Calculations were performed using the DFT scheme using the projector augmented-wave (PAW) method as implemented in the Vienna *Ab initio* Simulation Package (VASP) [47, 48]. The Perdew, Burke, and Ernzerhof (PBE) parametrization [28] of the GGA and the SCAN meta-GGA [36] were used for treating exchange correlation effects. The following valence electron configurations in the PAW potentials were chosen: Mn ($3s^23p^64s^23d^5$), V ($3s^23p^64s^23d^3$), Ge ($4s^23d^{10}4p^2$), and Si ($3s^23p^2$). The cut-off energy of 450 eV for the plane waves was used. The Monkhorst-Pack scheme [49] was applied for generating k-points in the reciprocal space. A grid of $11 \times 11 \times 11$ k-points was used in the relaxation procedure, while a grid of $25 \times 25 \times 25$ k-points was used in density-of-states (DOS) and band structure computations. Band structures for supercells were unfolded into the larger Brillouin zone for the primitive cell using the BandUP code [50, 51].

Geometry optimization for Mn-V-(Ge,Si) structures was carried out by taking into account both the static and atomic relaxations. The 16-atom cubic supercells based on the regular (space group $Fm\bar{3}m$) and inverse (space group $F\bar{4}3m$) Heusler structures were chosen for stoichiometric Mn$_2$VGe. Different magnetic orders such as FM, FIM, and AFM were considered for various crystal structures as illustrated in Fig. 1. The criteria for total energy convergence and residual atomic forces were set to 10^{-6} eV and 10^{-2} eV/Å, respectively.

To represent non-stoichiometric Mn$_2$VGe$_{1-x}$Si$_x$ compounds with Si content in the range of $0 < x \leq 0.5$, supercells were used as follows: 128 atoms for $x \approx 0.062$, 432 atoms for $x \approx 0.083$, 128 atoms for $x \approx 0.094$, 32 atoms for $x = 0.125$, 16 atoms for $x = 0.25$, 64 atoms for $x = 0.375$, and 16 atoms for $x = 0.5$. The chemical disorder between Ge and Si atoms was simulated using the special quasirandom

structure (SQS) scheme as implemented in the Alloy Theoretic Automated Toolkit (ATAT) package [52]. In order to predict the elastic properties and Debye temperatures from first principles, an analysis of the calculated total energies (E) of various compounds was carried out as a function of the applied strain (δ). The calculated $E(\delta)$ curves were fitted to a second-order polynomial $E(\delta) = E_0 + a_1\delta + a_2\delta^2$. Three types of cubic lattice distortions (isotropic, monoclinic, and orthorhombic) in the range of $-3\% \leq \delta \leq 3\%$ with a step of 1% were considered. The cubic elastic constants C_{11}, C_{12} and C_{44} were estimated from the second-order coefficient (a_2) using well-known relations [53]. The Debye temperature Θ_D was calculated from [54]

$$\Theta_D = \frac{\hbar}{k_B}\left[6n\pi^2\sqrt{V(T)}\right]^{1/3} f(\nu)\sqrt{\frac{B(T)N_A}{\mathcal{M}}},\tag{1}$$

where $\hbar$ is the reduced Planck constant, $\mathcal{M}$ is the molar mass, B is the bulk modulus, n is the number of atoms per unit cell, V is the cell volume, N_A is the Avogadro constant, and $f(\nu)$ is a function of the Poisson ratio ν which is given by

$$f(\nu) = \left\{3\left[2\left(\frac{2}{3}\frac{1+\nu}{1-2\nu}\right)^{3/2} + \left(\frac{1}{3}\frac{1+\nu}{1-\nu}\right)^{3/2}\right]^{-1}\right\}^{1/3}.\tag{2}$$

In order to investigate finite-temperature effects, Gibbs energy was calculated using [55]

$$G(V,P,T) = E(V) + PV(T) + F_{vib}(\Theta_D, T),\tag{3}$$

where $E(V)$ is the total energy as function of the volume V, P is the applied pressure, $F_{vib}(\Theta_D(V), T)$ is the vibration-free energy obtained within the Debye model

$$F_{vib}(\Theta_D, T) = nkT\left[\frac{9}{8}\frac{\Theta_D}{T} + 3\ln(1 - e^{-\Theta_D/T}) - D(\Theta_D/T)\right].\tag{4}$$

Here $D(\Theta_D/T)$ is the Debye function for an isotropic solid given by

$$D(x) = 3\left(\frac{T}{\Theta_D}\right)^3 \int_0^{\Theta_D/T} \frac{x^3}{e^x - 1}dx.\tag{5}$$

3 Results and discussion

3.1 Structural optimization of Mn$_2$VGe

First, we consider the geometry optimization of stoichiometric Mn$_2$VGe with regular and inverse Heusler structure considering different magnetic orders as illustrated in Fig 1. Total energy as a function of the lattice constant calculated using GGA and SCAN is presented in Figs. 2(a,b), respectively. The regular structure with FIM spin configuration is energetically the most favorable for both the GGA and SCAN. Interestingly, GGA yields a nearly degenerate non-magnetic (NM) phase at the same lattice parameter ($a_0 \approx 5.75$ Å) as for the FIM ground-state with an energy difference of about 11 meV/atom, which would be small enough to allow a transition between these two states with temperature. These results are in line with those based on the LSDA [13] although the GGA gives a larger lattice constant compared to the LSDA (5.65 Å). In contrast, SCAN yields the FIM–NM transition at $a_0 \approx 5.7$ Å can with a rather large energy difference of 45 meV/atom.

It is remarkable that in contrast to the GGA the SCAN FIM solution presents almost degenerate energy minima at $a_0 \approx 5.7$ and 6.0 Å . [A similar behavior has been recently predicted in Mn$_2$ScSi [38].] The left hand side energy minimum (blue curve in Fig. 2(b)) corresponds to the FIM state with a small but integral magnetic moment ($\mu_{tot} = 1.0$ μ_B/f.u.), while the right had side minimum represents the FIM state with a large magnetic moment ($\mu_{tot} = 4.778$ μ_B/f.u.). Following Ref. [38], we denote these states as LMS and HMS, respectively. Notably, both the SCAN and GGA values of μ_{tot} in the LMS obey
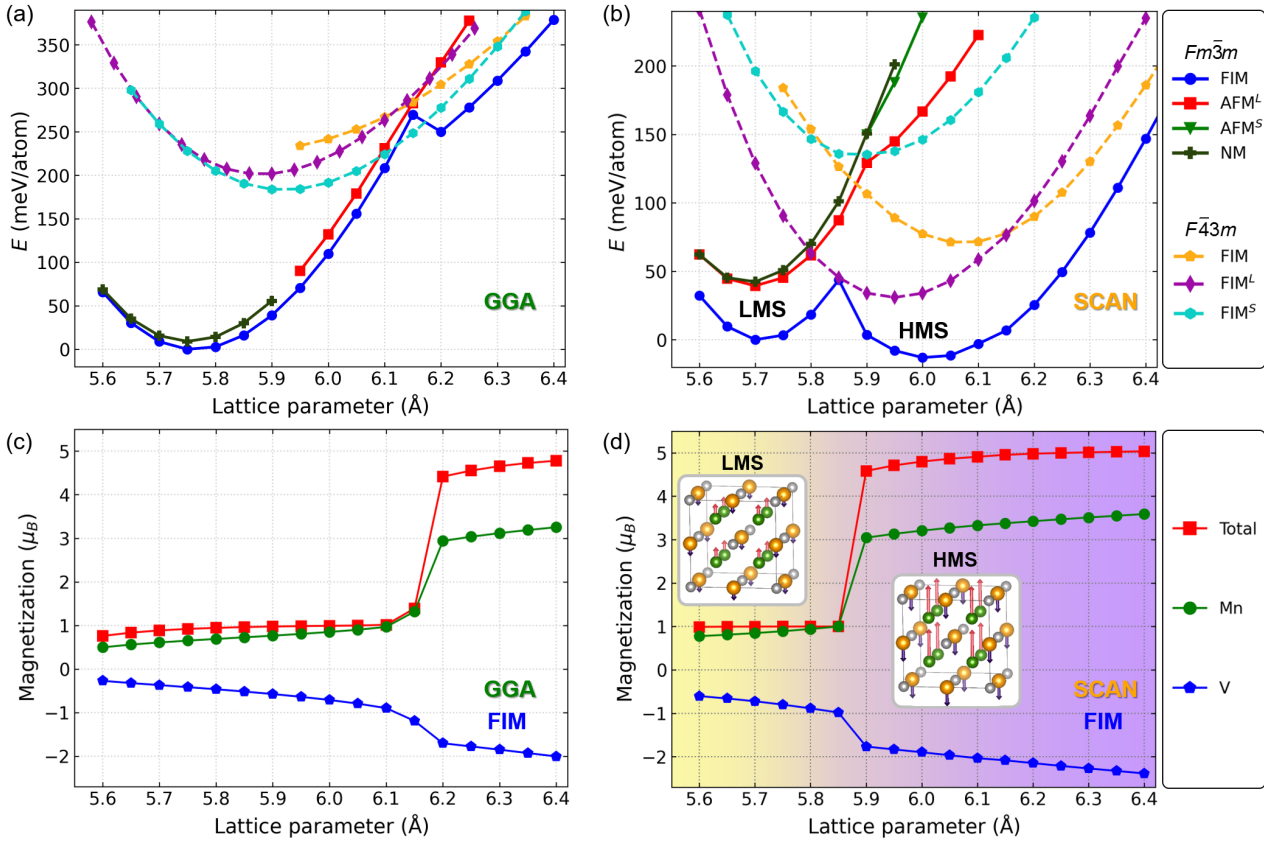
Figure 2: (a, b) The total energy E and (c, d) total and partial magnetic moments of Mn_2VGe as a function of the lattice parameter for GGA and SCAN solutions. The E zero is fixed to the LMS energy minimum in all cases.

the Slater-Pauling rule ($\mu_{tot} = |N_e - 24|$) in the HM Heusler alloys (add a reference to SP-rule), where N_e is the total number of valence electrons in the unit cell.

Figs. 2(c,d) illustrate the GGA and SCAN based total and partial magnetic moments for the FIM state as a function of the lattice parameter. Magnetic moments of Mn and V atoms are seen to align anti-parallel to produce the FIM order and change rapidly around ≈ 6.2 and 5.9 Å. In GGA, the jump-like behavior of μ_{tot} is followed by a small change in $E(a)$ (Fig. 2(a)). Electron correlations beyond the GGA captured in SCAN stabilize the HMS state at the larger volume. The SCAN yields the energy difference between LMS and HMS of $\Delta E \approx 13.2$ meV/atom, which is slightly larger compared to Mn_2ScSi [38].

3.2 Phase stability of Mn_2VGe

Due to possible martensitic transformations in Heusler compounds, it is important to consider effects of the tetragonal distortion in Mn_2VGe. In Fig. 3, the total energy difference with respect to the energy minimum of the cubic phase in LMS and HMS is plotted as a function of the tetragonal distortion c/a. For GGA, only one $E(c/a)$ curve is shown corresponding to the energy minimum in Fig. 2(a). The GGA solution does not provide any minima for $c/a \neq 1$ indicating the stability of the cubic austenitic phase. SCAN, however, yields both the LMS and HMS cubic phases and demonstrates a pseudo-martensitic behavior at c/a ratios of 1.25 and 1.3, where the tetragonally distorted HMS has a lower energy, although it is 115 meV/atom higher in energy than the cubic phase, which is the most stable global phase of Mn_2VGe. Next, we discuss the elastic properties of Mn_2VGe given in Table 1. The Born-Huang stability criterion [56] ($C_{11} > 0$; $C_{12} > 0$; $C_{44} > 0$; $C_{11} > C_{12}$; $C_{11} + C_{12} > 0$) is satisfied in Mn_2VGe, which indicates that the compound is mechanically stable. Another important property is given by the Zener anisotropy coefficient ($A = C_{44}/C'$) [57], which determines the structural stability and the probability of microcrack formation in the material. A small elastic anisotropy is found in the LMS phase in both GGA and SCAN, although SCAN gives a five times larger value. The Poisson ratio ν is a measure of the
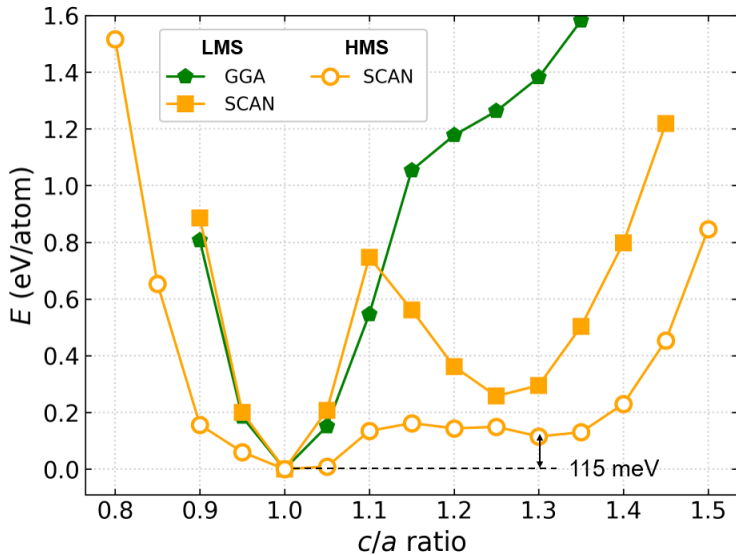
Figure 3: GGA and SCAN total energies as a function of the tetragonal distortion in Mn_2VGe for the regular Heusler structure ordered ferrimagnetically (FIM). The energy zero refers to the energy of the cubic phase in all cass.

Table 1: Calculated elastic properties of Mn_2VGe: the bulk modulus B (in GPa), shear elastic constant C' (in GPa), elastic constants C_{ij} (in GPa), anisotropy Zener ratio A, Poisson ratio ν, Young's modulus E_Y (in GPa), and the Debye temperature Θ_D (in K). Here XC denotes the exchange correlation functional.

Magnetic state	XC	B	C'	C_{11}	C_{12}	C_{44}	A	ν	E_Y	Θ_D
LMS	GGA	229.9	84.5	342.6	173.6	136.3	1.61	0.29	290.2	540.6
	SCAN	257.3	109.5	403.2	184.3	158.8	1.45	0.27	348.6	592.6
HMS	SCAN	121.6	14.0	140.3	112.2	112.2	8.01	0.32	134.7	373.3

ductility or brittleness: a material is considered ductile if $\nu > 0.26$, otherwise it is brittle [53]. All phases of Mn_2VGe are predicted to be ductile for both GGA and SCAN. Stiffness of a material is described by the Young's modulus (E_Y). When LMS changes to HMS within the SCAN calculations, Young's modulus decreases significantly and the softness increases. The calculated tetragonal shearing coefficient C' is larger than that of Ni_2MnGa that exhibits an austenite-martensite transformation. [The calculated C' for Ni_2MnGa is about 5.5 GPa [58] compared to the experimental value of 4.5 GPa [59].] The larger C' value is consistent with the absence of a tetragonal transition in Mn_2VGe. Our GGA results are generally similar to those of Ram *et al.* [35] for Mn_2ScZ (Z = Si, Ge, Sn) and Huang *et al.* [60] for the quaternary CoMnVTe Heusler alloy.

In order to examine the possibility of segregation, we carried out a convex-hull analysis [61] using formation energies. Note that the convex hull represents the surface of minimum formation energy for a set of ground state configurations in the composition space. Compounds located above the convex hull are unstable to decomposition into other more stable compounds. We constructed the convex hull surface for Mn-V-Ge by considering seven stable binary compounds (pivot points) together with Mn_2VGe. The SCAN-based results are shown in the contour map of Fig. 4, where Mn_2VGe has the lowest formation energy in the convex hull. Crystal and magnetic structures and the formation energies for GGA and SCAN are given in Table 2. The alloy is thus predicted to be chemically stable against segregation into pure elements and binary compounds suggesting that it will be amenable to relatively easy synthesis. Similar results for the GGA are given in the Materials Project and AFLOW databases [62, 61]. NOTE: I have removed reference to Materials Project and AFLOW in the caption below–arun

Finally, we discuss possible transitions between the LMS and HMS phases with temperature and external pressure. In this connection, Fig. 5 presents the Gibbs energy difference between these two phases. [Debye temperatures are listed in Table 1.] Here we neglect the magnetic and electronic contributions to the entropy for the sake of simplicity. No transitions are predicted below 3 GPa. At higher pressures, the transition temperature is seen to vary linearly with increasing pressure, see Fig. 5. A pressure of $\approx$
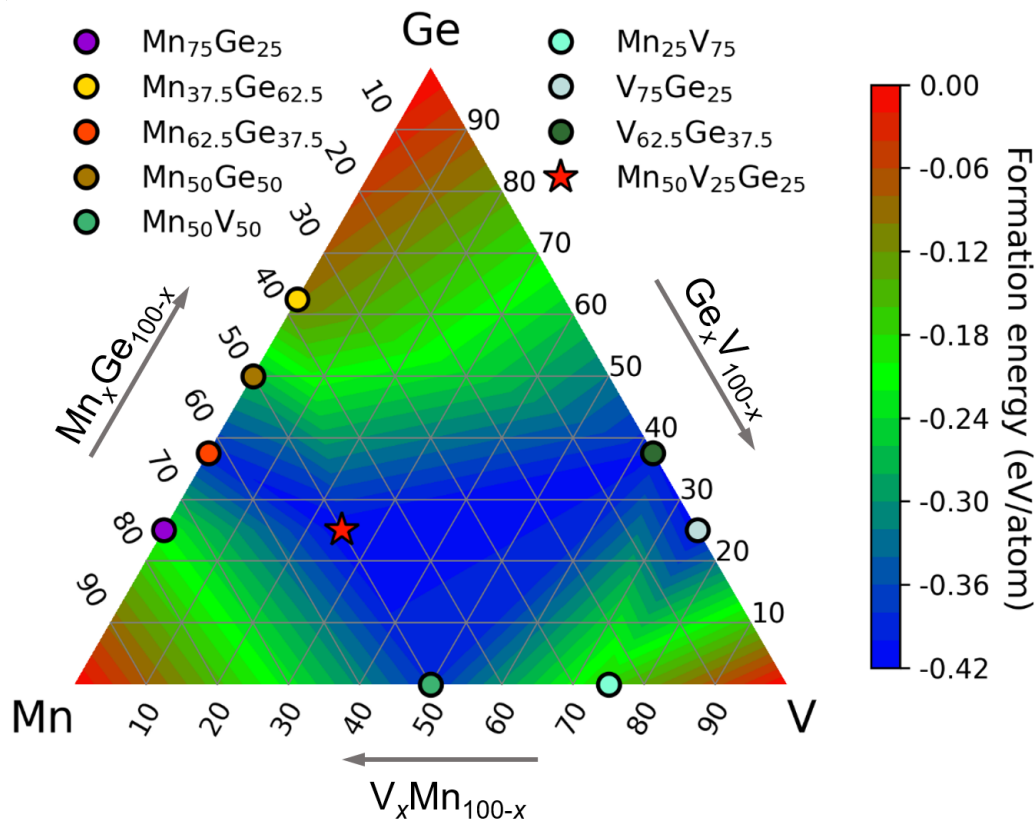
Figure 4: Energy convex-hull diagram for the ternary Mn-V-Ge system calculated within SCAN.

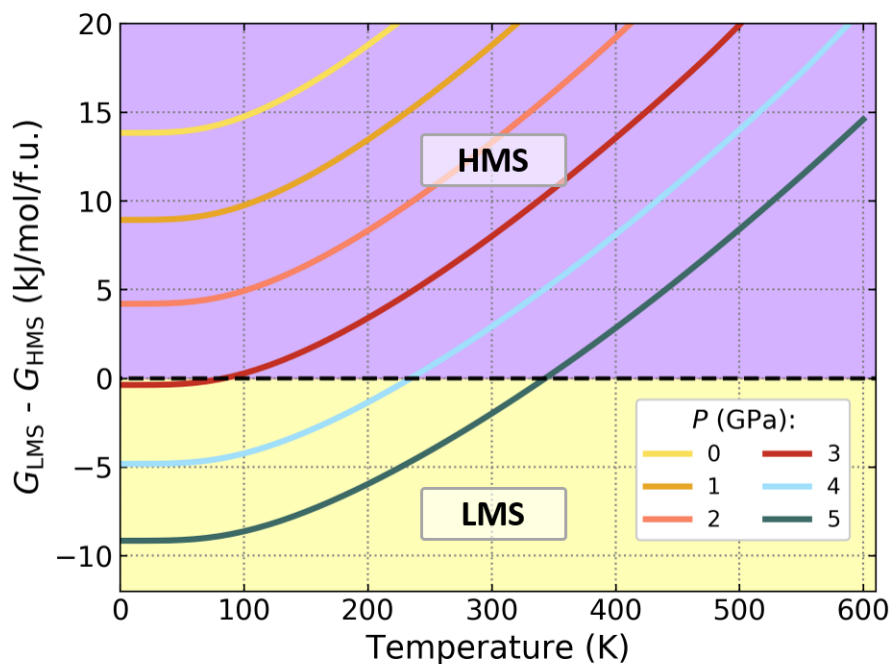4 GPa is necessary for switching between LMS and HMS at the room temperature.

Figure 5: Temperature dependence of the Gibbs energy difference between LMS and HMS for Mn_2VGe for various values of the applied pressure P.

Table 2: Space groups, magnetic orderings, total magnetic moments (in μ_B/f.u.), and formation energies (in meV/atom) for the pivot points of the ternary Mn-V-Ge convex hull using GGA and SCAN. For Mn$_2$VGe, the results for both crystal structures and various magnetic configurations given in Fig. 2(b) are presented: the most favorable phase is marked in bold lettering.

	Space group	Magnetic ordering	Magnetic moment		Formation energy	
			GGA	SCAN	GGA	SCAN
Mn	217	FIM	0.18	0.46	0.00	0.00
V	229	NM	0.01	0.00	0.00	0.00
Ge	227	NM	0.00	0.00	0.00	0.00
Mn$_3$Ge	225	FM	2.65	2.81	-0.08	-0.22
Mn$_5$Ge$_3$	193	FM	13.23	14.85	-0.11	-0.39
Mn$_3$Ge$_5$	118	FIM	1.00	0.98	0.01	-0.10
MnGe	198	FM	2.003	2.16	-0.12	-0.27
MnV	221	NM	0.00	0.00	-0.28	-0.38
MnV$_3$	225	NM/FIM	0.01	0.92	-0.15	-0.17
V$_3$Ge	223	FM/NM	0.35	0.01	-0.34	-0.41
V$_5$Ge$_3$	140	NM/FIM	0.00	1.82	-0.37	-0.40
	225	FIM (LMS)	0.99	1.00	-0.28	-0.42
	225	**FIM (HMS)**	**–**	**4.78**	**–**	**-0.43**
	225	NM	0.00	0.00	-0.20	-0.37
Mn$_2$VGe	225	AFM^L	–	0.00	–	-0.38
	216	FIM	0.57	4.58	0.02	-0.34
	216	FIM^L	0.00	0.88	0.00	-0.39
	216	FIM^S	0.57	0.00	-0.02	-0.28

3.3 Electronic structure of Mn$_2$VGe

In order to understand the influence of electron correlations on the electronic structure of Mn$_2$VGe further, we compare in Fig. 6, the spin-polarized band structures, and the total and partial DOSs of the LMS and HMS phases at their equilibrium lattice constants. For the LMS, both GGA and SCAN predict a metallic character with bands crossing the Fermi level in the minority spin channel and the minority spins of Mn host a large DOS at E_F. In contrast, the majority spin band differs somewhat between the GGA and SCAN. GGA gives an almost HM behavior at E_F due to a presence of a valence band maximum at Γ, which lies ≈ 0.25 eV above E_F with a spin polarization of about 90%. In SCAN, there are direct majority band gaps at E_F with values of $E_{\Gamma-\Gamma} = 1.104$ eV, $E_{X-X} = 1.201$ eV and an indirect gap $E_{\Gamma-X} = 0.580$ eV. Remarkably, the Fermi energy is located at the center of the energy gap, yielding a stable half-metallic state with 100 % spin polarization under applied pressure. The band gap is mostly determined by the contribution of Mn orbitals. Note also that the pDOS (partial DOS) for V atoms is quite symmetric and, therefore, V has a small magnetic moment relative to the Mn atoms. For a larger cell volume, both the majority and minority bands intersect E_F and result in a metallic HMS phase. The presence of HM and metallic phases at different volumes would allow switching of spin-polarized current to spin-unpolarized current with pressure.

Fig. 7 presents SCAN-based pDOS's for Mn and V in the LMS and HMS phases. It is clear that the predominant contribution to the band gap at the Fermi level of the LMS phase is from the t_{2g} Mn orbitals, with a smaller contribution from the Mn e_g orbitals. Similar arguments for the formation of a semiconducting gap in Heusler alloys have been made for Co$_2$MnGe, Mn$_2$ScZ and Fe$_2$TiZ (Z = Ga, Ge, As, In, Sn, and Sb) [63, 35, 64]. On the other hand, the metallic nature of the HMS phase is determined by the occupation of e_g and t_{2g} Mn orbitals in both spin channels. Also, the valence band in the LMS as well as HMS is characterized by an almost equal occupation of both e_g and t_{2g} Mn orbitals, while the e_g Mn electrons dominate the occupation of the conduction band. Concerning the V atoms, the t_{2g} orbitals contribute to the valence band of LMS and HMS whereas both the e_g and t_{2g} orbitals are occupied in the conduction band. We thus conclude that the t_{2g} states mostly contribute to the LMS, while in the HMS both t_{2g} and e_g are involved. For V, the e_g states in the conduction band are responsible for the magnetic moment of both LMS and HMS. Interestingly, in Mn$_2$ScSi [38], Sc gives much smaller magnetic
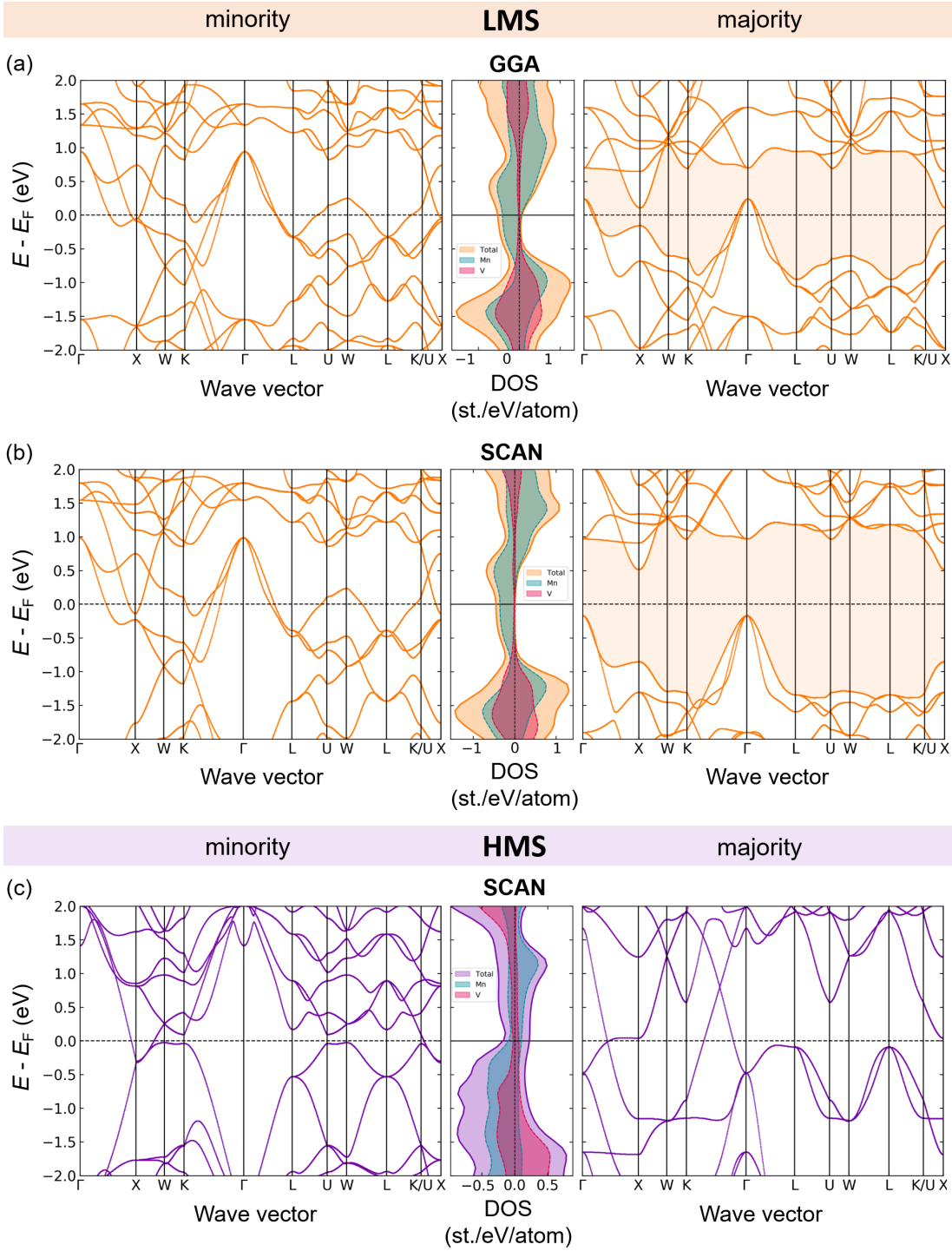
Figure 6: Majority and minority band structures and total and partial DOSs for Mn_2VGe. (a) GGA results for LMS. (b,c) SCAN results for (b) LMS and (c) HMS at their equilibrium volumes.

contribution compared to V.

Previous *ab initio* GGA studies [8] of Mn_2TiZ (Z = Al, As, Bi, Ga, Ge, Sb, Si, and Sn) Have found that an expansion of the lattice raises the Fermi level to higher energies through the semimetallic gap with little change in spin polarization of the states or the size of the energy gap. In contrast, in our case here the loss of half-metallicity in Mn_2VGe with volume expansion as the system transitions to the HMS phase is associated with a significant reshuffling of the electronic states.
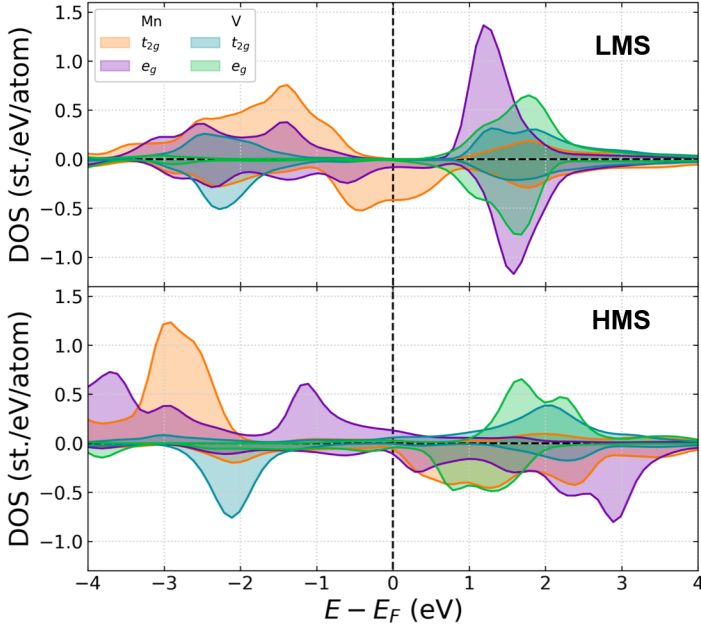
Figure 7: Orbitally-resolved DOSs of Mn and V atoms in the LMS and HMS Mn$_2$VGe using SCAN.

3.4 Si-doped Mn$_2$VGe

Substitution of Ge with Si can tune the energy difference ΔE between the LMS and HMS phases as shown in Fig. 8 for a series of alloy compositions simulated using supercells of various sizes. Large, computationally expensive supercells are required for low Si concentration x: The largest supercell we deployed involved 432 atoms for $x \approx 0.083$. ΔE is seen in Fig. 8 to vary linearly with x. For x less than 0.1 (3 at.%), HMS is the global minimum while for larger x, the LMS becomes the global minimum. We thus conclude that LMS and HMS become degenerate at zero temperature for Si concentration of about 2.92 at.% ($x \approx 0.17$). Further increase of Si content raises ΔE significantly.

In order to identify an alloy composition at which the LMS/HMS switching would become easier ($\Delta E \approx 0$ meV/atom), we focus on a 32-atom supercell ($x = 0.125$). In this case, Fig. ?? shows the presence of two nearly-degenerate minima (green filled squares). A small amount of Si ($x = 0.125$ at.%) is seen (Fig. 9(a)) to result in a substantial decrease in —ΔE— from 13.2 to 3.1 meV/atom. Notably, with full geometry optimization and relaxation of atomic positions —ΔE— reduces from 3.1 to 1.8 meV/atom at $x = 0.125$ at.%. Since the DOSs in the Si alloys are very similar to those of the parent compound (see Figs. 7 and 9(b)), the rigid band approximation is reasonable for modeling the electronic structures of these alloys.

Finally, Fig. 10 presents transition pressures (P_{tr}) to switch from LMS to HMS as a function of Si content at temperatures (T_{tr}) of 0 K, liquid nitrogen and the room temperature. Both P_{tr} and T_{tr} have been estimated here from the intersection of Gibbs energies of the LMS and HMS phases. At each composition, Θ_D for LMS and HMS was determined via a linear interpolation of the values for $x = 0$ ($\Theta_D^{LMS} \approx$ 593 K and $\Theta_D^{HMS} \approx 373$ K) and $x = 0.5$ ($\Theta_D^{LMS} \approx 625$ K and $\Theta_D^{HMS} \approx 419$ K). By increasing the Si concentration, we can control the pressure required for the magnetic transition between HMS and LMS. A positive P_{tr} (lattice contraction) activates the HMS $\rightarrow$ LMS transition while a negative P_{tr} (lattice expansion) stimulates the LMS $\rightarrow$ HMS transition. For example, at zero temperature and room temperature, a pressure of only 1 and 2.8 GPa, respectively, is required to trigger the transition at $x = 0.125$. Increasing Si content reduces the transition pressure, which is seen to nearly become zero at $x \approx 0.45$ at room temperature.
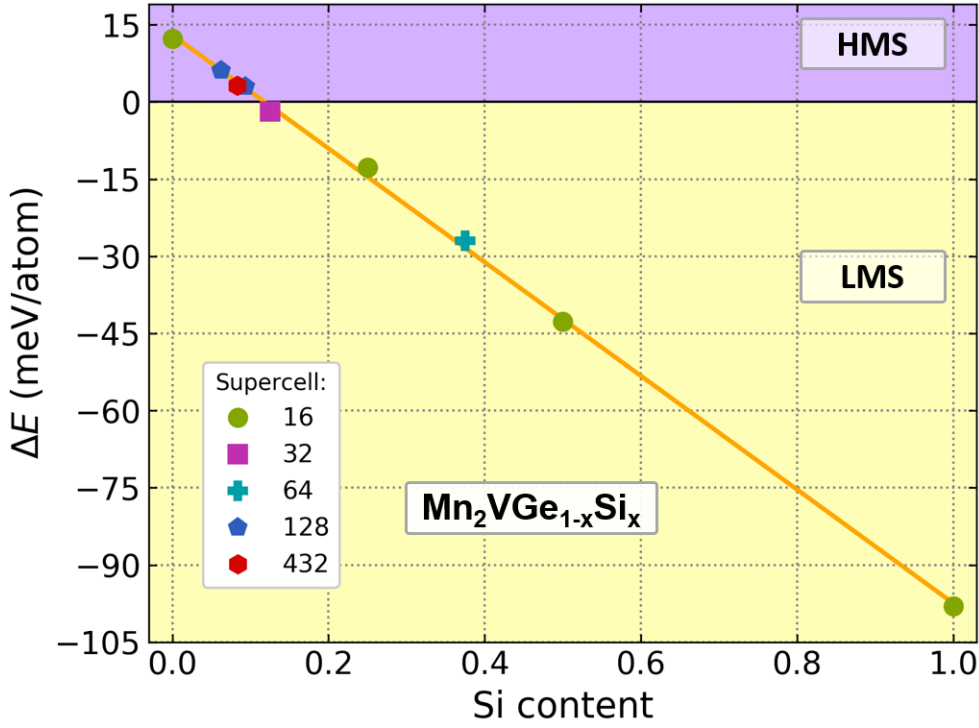
Figure 8: Energy difference between the LMS and HMS phases as a function of Si content for $Mn_2VGe_{1-x}Si_x$ alloys. Various alloy compositions are simulated by generating SQS supercells with different number of atoms. Orange line gives the linear approximation.
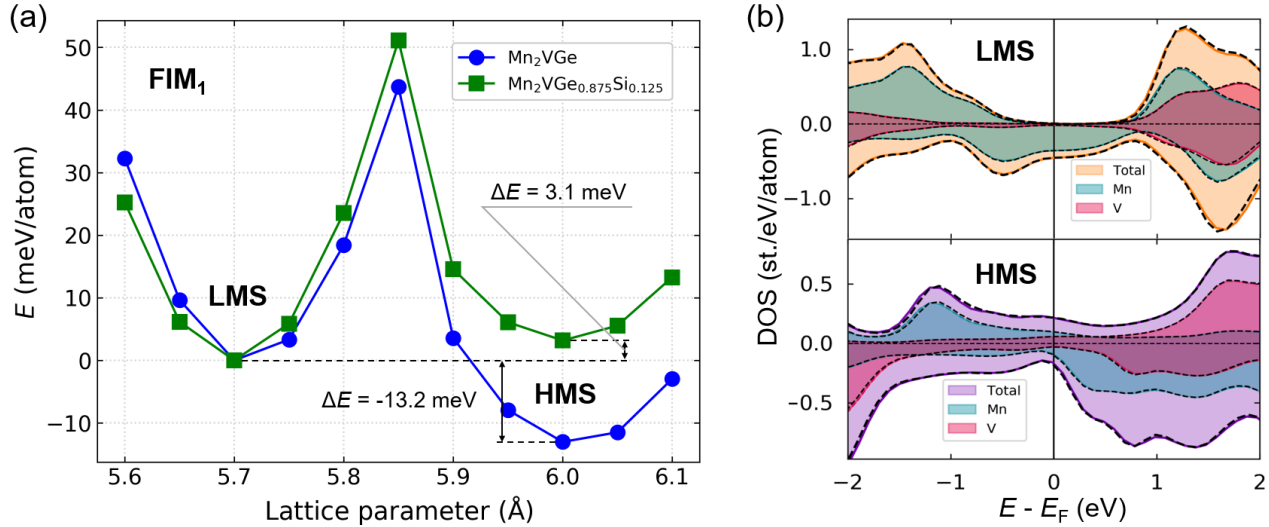

Figure 9: (a) SCAN-based total energy as a function of the lattice parameter for Mn_2VGe and $Mn_2VGe_{0.875}Si_{0.125}$ ($Mn_{16}V_8Ge_7Si_1$) with FIM order. The E zero is fixed to the LMS energy minimum in all cases. (b) Total and partial DOSs of $Mn_2VGe_{0.875}Si_{0.125}$ in the LMS and HMS phases calculated at the corresponding equilibrium volumes. Dashed lines are for Mn_2VGe.

4 Conclusion

We present an in-depth study of spin-dependent electronic structures of Si-doped Mn_2VGe alloys, which are easy to synthesize and promising for spintronics applications, using the SCAN meta-GGA functional within the first-principles density functional theory framework. The total energy curves for these compounds are found to consist of two distinct branches with small energy differences between their minima. The minimum corresponding to the larger equilibrium unit-cell volume hosts a phase with high total magnetic moment and a fully metallic band structure. The minimum with a smaller cell volume, how-
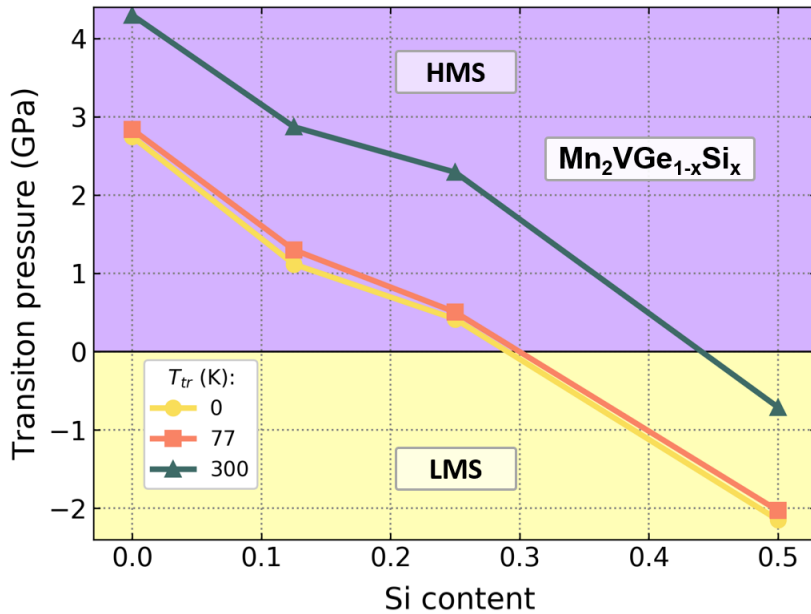
11

Figure 10: Transition pressure for switching between the LMS and HMS phases as a function of the Si content.

ever, yields a half-metallic phase with a smaller total magnetic moment. Substitution of Ge by Si results in the reduction of the energy difference between the metallic and half-metallic phases, and these two phases become nearly degenerate at a Si concentration of 0.125% at zero temperature.

Supporting Information
Supporting Information is available from the Wiley Online Library or from the author.

Acknowledgements

References

[1] W. Gallagher, *Emerging Spintronic Memories*, CRC Press, **2019**.

[2] A. Fert, *Rev. Mod. Phys.* **2008**, *80*, 4 1517.

[3] B. Dieny, I. L. Prejbeanu, K. Garello, P. Gambardella, P. Freitas, R. Lehndorff, W. Raberg, U. Ebels, S. O. Demokritov, J. Akerman, et al., *Nat. Electron.* **2020**, *3*, 8 446.

[4] J. Puebla, J. Kim, K. Kondou, Y. Otani, *Commun. Mater.* **2020**, *1*, 1 1.

[5] S. P. Lewis, P. B. Allen, T. Sasaki, *Phys. Rev. B* **1997**, *55*, 16 10253.

[6] H. Akai, *Phys. Rev. Lett.* **1998**, *81*, 14 3002.

[7] H. Luo, Z. Zhu, G. Liu, S. Xu, G. Wu, H. Liu, J. Qu, Y. Li, *J. Magn. Magn. Mater.* **2008**, *320*, 3-4 421.

[8] H. Zenasni, H. Faraoun, C. Esling, *J. Magn. Magn. Mater.* **2013**, *333* 162.

[9] D. Hoat, J. Rivas-Silva, A. M. Blas, *J. Comput. Electron.* **2018**, *17*, 4 1470.

[10] C. Jiang, M. Venkatesan, J. Coey, *Solid State Commun.* **2001**, *118*, 10 513.

[11] R. Weht, W. E. Pickett, *Phys. Rev. B* **1999**, *60*, 18 13006.

[12] R. Umetsu, H. Fujiwara, K. Nagai, Y. Nakatani, M. Kawada, A. Sekiyama, F. Kuroda, H. Fujii, T. Oguchi, Y. Harada, et al., *Phys. Rev. B* **2019**, *99*, 13 134414.

[13] K. Özdogan, I. Galanakis, E. Şaşioglu, B. Aktaş, *J. Condens. Matter Phys.* **2006**, *18*, 10 2905.

[14] H. Luo, H. Zhang, Z. Zhu, L. Ma, S. Xu, G. Wu, X. Zhu, C. Jiang, H. Xu, *J. Appl. Phys.* **2008**, *103*, 8 083908.

[15] Y. Li, G. Liu, X. Wang, E. Liu, X. Xi, W. Wang, G. Wu, L. Wang, X. Dai, *Results Phys.* **2017**, *7* 2248.

[16] S. Ouardi, G. H. Fecher, C. Felser, J. Kübler, *Phys. Rev. Lett.* **2013**, *110* 100401.

[17] A. Jakobsson, P. Mavropoulos, E. Şaşıoğlu, S. Blügel, M. Ležaić, B. Sanyal, I. Galanakis, *Phys. Rev. B* **2015**, *91*, 17 174439.

[18] S. Skaftouros, K. Özdoğan, E. Şaşıoğlu, I. Galanakis, *Appl. Phys. Lett.* **2013**, *102*, 2 022402.

[19] X.-R. Chen, M.-M. Zhong, Y. Feng, Y. Zhou, H.-K. Yuan, H. Chen, *Phys. Status Solidi B* **2015**, *252*, 12 2830.

[20] Y. Feng, T. Zhou, X. Chen, H. Yuan, H. Chen, *J. Phys. D: Appl. Phys.* **2015**, *48*, 28 285302.

[21] M. Meinert, J.-M. Schmalhorst, G. Reiss, *J. Condens. Matter Phys.* **2010**, *23*, 3 036001.

[22] H. Luo, G. Liu, F. Meng, L. Wang, E. Liu, G. Wu, X. Zhu, C. Jiang, *Comput. Mater. Sci.* **2011**, *50*, 11 3119.

[23] A. Abada, K. Amara, S. Hiadsi, B. Amrani, *J. Magn. Magn. Mater.* **2015**, *388* 59.

[24] K. R. Kumar, J. A. Chelvane, G. Markandeyulu, S. Malik, N. H. Kumar, *Solid State Commun.* **2010**, *150*, 1-2 70.

[25] R. M. Martin, *Electronic Structure: Basic Theory and Practical Methods*, Cambridge University Press, **2004**.

[26] B. Barbiellini, E. Moroni, T. Jarlborg, *J. Condens. Matter Phys.* **1990**, *2*, 37 7597.

[27] J. P. Perdew, Y. Wang, *Phys. Rev. B* **1992**, *45*, 23 13244.

[28] J. Perdew, K. Burke, M. Ernzerhof, *Phys. Rev. Lett.* **1996**, *77* 3865.

[29] I. Galanakis, K. Özdoğan, E. Şaşıoğlu, B. Aktaş, *Phys. Rev. B* **2007**, *75*, 9 092407.

[30] G. Liu, X. Dai, H. Liu, J. Chen, Y. Li, G. Xiao, G. Wu, *Phys. Rev. B* **2008**, *77*, 1 014424.

[31] S. Li, Z. Ren, X. Zhang, C. Cao, *Physica B: Condensed Matter* **2009**, *404*, 14-15 1965.

[32] X.-P. Wei, X.-R. Hu, G.-Y. Mao, S.-B. Chu, T. Lei, L.-B. Hu, J.-B. Deng, *J. Magn. Magn. Mater.* **2010**, *322*, 20 3204.

[33] X.-P. Wei, X.-R. Hu, S.-B. Chu, G.-Y. Mao, L.-B. Hu, T. Lei, J.-B. Deng, *Physica B: Condensed Matter* **2011**, *406*, 5 1139.

[34] D. Bensaid, T. Hellal, M. Ameri, Y. Azzaz, B. Doumi, Y. Al-Douri, B. Abderrahim, F. Benzoudji, *J. Supercond. Nov. Magn.* **2016**, *29*, 7 1843.

[35] M. Ram, A. Saxena, A. E. Aly, A. Shankar, *RSC Adv.* **2020**, *10*, 13 7661.

[36] J. Sun, A. Ruzsinszky, J. P. Perdew, *Phys. Rev. Lett.* **2015**, *115* 036402.

[37] J. Sun, R. C. Remsing, Y. Zhang, Z. Sun, A. Ruzsinszky, H. Peng, Z. Yang, A. Paul, U. Waghmare, X. Wu, et al., *Nature chemistry* **2016**, *8*, 9 831.

[38] V. D. Buchelnikov, V. V. Sokolovskiy, O. N. Miroshkina, D. R. Baigutlin, M. A. Zagrebin, B. Barbiellini, E. Lähderanta, *Phys. Rev. B* **2021**, *103*, 5 054414.

[39] D. A. Kitchaev, H. Peng, Y. Liu, J. Sun, J. P. Perdew, G. Ceder, *Phys. Rev. B* **2016**, *93* 045132.

[40] I.-G. Buda, C. Lane, B. Barbiellini, A. Ruzsinszky, J. Sun, A. Bansil, *Scientific reports* **2017**, *7*, 1 1.

[41] C. Lane, J. W. Furness, I. G. Buda, Y. Zhang, R. S. Markiewicz, B. Barbiellini, J. Sun, A. Bansil, *Phys. Rev. B* **2018**, *98* 125140.

[42] J. W. Furness, Y. Zhang, C. Lane, I. G. Buda, B. Barbiellini, R. S. Markiewicz, A. Bansil, J. Sun, *Commun Phys* **2018**, *1* 11.

[43] Y. Zhang, C. Lane, J. W. Furness, B. Barbiellini, R. S. Markiewicz, A. Bansil, J. Sun, Landscape of competing stripe and magnetic phases in cuprates, **2018**.

[44] A. Pulkkinen, B. Barbiellini, J. Nokelainen, V. Sokolovskiy, D. Baigutlin, O. Miroshkina, M. Zagrebin, V. Buchelnikov, C. Lane, R. S. Markiewicz, A. Bansil, J. Sun, K. Pussi, E. Lähderanta, *Phys. Rev. B* **2020**, *101* 075115.

[45] V. D. Buchelnikov, V. V. Sokolovskiy, O. N. Miroshkina, M. A. Zagrebin, J. Nokelainen, A. Pulkkinen, B. Barbiellini, E. Lähderanta, *Phys. Rev. B* **2019**, *99* 014426.

[46] O. N. Miroshkina, D. R. Baigutlin, V. V. Sokolovskiy, M. A. Zagrebin, A. Pulkkinen, B. Barbiellini, E. Lähderanta, V. D. Buchelnikov, *J. Appl. Phys.* **2020**, *127*, 17 175108.

[47] G. Kresse, J. Furthmüller, *Phys. Rev. B* **1996**, *54* 11169.

[48] G. Kresse, D. Joubert, *Phys. Rev. B* **1999**, *59* 1758.

[49] H. J. Monkhorst, J. D. Pack, *Phys. Rev. B* **1976**, *13*, 12 5188.

[50] P. V. Medeiros, S. Stafström, J. Björk, *Phys. Rev. B* **2014**, *89*, 4 041407.

[51] P. V. Medeiros, S. S. Tsirkin, S. Stafström, J. Björk, *Phys. Rev. B* **2015**, *91*, 4 041116.

[52] A. Van de Walle, P. Tiwary, M. De Jong, D. Olmsted, M. Asta, A. Dick, D. Shin, Y. Wang, L.-Q. Chen, Z.-K. Liu, *Calphad* **2013**, *42* 13.

[53] I. Frantsevich, F. Voronov, S. Bakuta, *Kiev, Izdatel'stvo Naukova Dumka, 1982, 288* **1982**.

[54] M. Zagrebin, V. Sokolovskiy, V. Buchelnikov, *J. Phys. D: Appl. Phys.* **2016**, *49*, 35 355004.

[55] V. Moruzzi, J. Janak, K. Schwarz, *Phys. Rev. B* **1988**, *37*, 2 790.

[56] M. Born, K. Huang, *Publishers, Berlin* **1982**.

[57] C. Zener, *Physical Review* **1951**, *82*, 3 403.

[58] S. O. Kart, T. Cagın, *Journal of Alloys and Compounds* **2010**, *508*, 1 177.

[59] J. Worgull, E. Petti, J. Trivisonno, *Phys. Rev. B* **1996**, *54*, 22 15695.

[60] H. Huang, H. Zhou, G. Liu, A. Laref, L. Liu, *Applied Physics A* **2020**, *126*, 11 1.

[61] C. Oses, E. Gossett, D. Hicks, F. Rose, M. J. Mehl, E. Perim, I. Takeuchi, S. Sanvito, M. Scheffler, Y. Lederer, et al., *J. Chem. Inf. Model.* **2018**, *58*, 12 2477.

[62] A. Jain, S. P. Ong, G. Hautier, W. Chen, W. D. Richards, S. Dacek, S. Cholia, D. Gunter, D. Skinner, G. Ceder, K. a. Persson, *APL Materials* **2013**, *1*, 1 011002.

[63] I. Galanakis, P. Mavropoulos, P. H. Dederichs, *J. Phys. D* **2006**, *39*, 5 765.

[64] H. Luo, G. Liu, F. Meng, J. Li, E. Liu, G. Wu, *J. Magn. Magn. Mater.* **2012**, *324*, 20 3295.